

# Spatio-temporal stability of the laminar stratified Ekman layer

Aaron Wienkers & Sanjiva Lele

## 1 Introduction

The Coriolis force is often an important dynamical influence on geophysical scales such in astrophysical discs, solar atmospheres, or in planetary boundary layers. In a non-inertial local reference frame spinning with the Earth, a steady state solution exists high in the atmosphere from the geostrophic balance between pressure gradients and the Coriolis force. However, friction required to satisfy the no-slip condition on the surface of the Earth means that an additional force comes into this balance, resulting in an *Ekman spiral* with decreasing height. This particular Ekman layer solution was first found by Ekman in 1905. Contrasting to the classical two-dimensional Blasius boundary layer profile, this base state is already three-dimensional, which will pose new analytic challenges.

The temporal stability of this Ekman base flow is by now well-known, as is the analysis for the extension to a stratified layer (Brown, 1972). This temporal formulation studying the growth of spatially-periodic perturbations with time is contrasted with spatial stability analysis which considers spatial growth of localised (in space) time-oscillatory perturbations of a certain frequency. Although the analysis of temporal stability is typically more straightforward, in experiments as well as in nature, the spatial development following localised perturbations is more appropriate. For example, the response to a vibrating ribbon in a boundary layer is the classic example of such spatial analyses (Gaster, 1965; Ashpis & Reshotko, 1990). There is typically no straightforward mapping between the temporal and spatial growth rates, except in special cases. One such particular regime was pointed out by Gaster (1962) which linearises the dispersion relation, and thus holds only for marginally unstable flows. This is the approach taken by Marlatt & Biringen (1994) to calculate the spatial modes in the unstratified Ekman layer; however, it is only really accurate near the neutral stability boundary.

This work seeks to extend the approximate results of Marlatt & Biringen (1994), as well as generalise the resulting analysis to include the effects of stratification. We start by reformulating the theory in §2, whereafter we present our numerical procedure to calculate the spatio-temporal stability in §3. We then proceed to validate our results over a range of pertinent test cases, including reduction to the Blasius boundary layer, as well as recovering the analytically-determined continuous spectra. Finally, in §4 we present and discuss the effects of stratification on damping the most unstable temporal and spatial modes.

## 2 Physical model

### 2.1 Governing system

A local cartesian but non-inertial frame,  $(x, y, z)$ , is entered at latitude  $\lambda$  on a rotating manifold representing the northern hemisphere of a planetary atmosphere. Using the Boussinesq approximation and assuming an adiabatic but thermally diffusive fluid, the governing set may be written as

$$\frac{\partial \mathbf{u}}{\partial t} + \mathbf{u} \cdot \nabla \mathbf{u} = -\frac{\nabla \Pi}{\rho_0} - 2\boldsymbol{\Omega} \times (\mathbf{u} - \mathbf{G}) + \nu \nabla^2 \mathbf{u} + b\hat{\mathbf{z}} \quad (1a)$$

$$\frac{\partial \theta}{\partial t} + \mathbf{u} \cdot \nabla \theta = \kappa \nabla^2 \theta. \quad (1b)$$

Here the buoyancy force is

$$b = -g \frac{\rho - \rho_0}{\rho_0} \approx g \frac{\theta - \bar{\theta}(z)}{\theta_0} \quad (2)$$

where  $\theta$  is the potential temperature defined as

$$\theta \equiv T \left( \frac{p}{p_0} \right)^{\frac{\gamma-1}{\gamma}}. \quad (3)$$

With the stratification set by the background potential temperature,  $\bar{\theta}$ , the buoyancy frequency may be further defined as

$$N(z) \equiv \sqrt{\frac{g}{\theta_0} \frac{\partial \bar{\theta}}{\partial z}}. \quad (4)$$

The geostrophic force balance between the Coriolis force arising due to the free-stream large scale motions,  $\mathbf{G} = G \cos(\alpha)\hat{\mathbf{x}} + G \sin(\alpha)\hat{\mathbf{y}}$ , and the

horizontal pressure gradient is absorbed into the pressure term, and will be quickly eliminated in this local frame by a Helmholtz decomposition. After a further simplification by rotating the coordinate system by an angle  $\varepsilon$  to the north of the geostrophic wind angle, the nondimensionalised Boussinesq system becomes

$$\frac{\partial \mathbf{u}^*}{\partial t^*} + \mathbf{u}^* \cdot \nabla^* \mathbf{u}^* = -\frac{\nabla^* \Pi}{\rho_0^*} - 2\boldsymbol{\Omega}^* \times \left( \mathbf{u}^* - \frac{\mathbf{G}}{G} \right) + \frac{1}{\text{Re}} \nabla^{*2} \mathbf{u}^* + \theta^* \hat{\mathbf{z}} \quad (5a)$$

$$\frac{\partial \theta^*}{\partial t^*} + \mathbf{u}^* \cdot \nabla^* \theta^* = -\frac{\mathbf{u}^*}{\text{Fr}^2} \cdot \nabla \left( \frac{\bar{\theta}}{\theta_0} \right) + \frac{1}{\text{RePr}} \nabla^2 \left( \theta^* + \frac{1}{\text{Fr}^2} \frac{\bar{\theta}}{\theta_0} \right). \quad (5b)$$

We define the local Richardson number as

$$\text{Ri}_l = \frac{g \partial_z \bar{\theta}}{\theta_0} \frac{D}{G^2} = gS \frac{D}{G^2} = \frac{S}{\text{Fr}^2}, \quad (6)$$

so that the background stratification can either be prescribed using  $S(z)$  and  $\text{Fr}$ , or solely with  $\text{Ri}_l(z)$ . The length-scale used to write (5) is the Ekman layer depth,

$$D \equiv \sqrt{\frac{\nu}{\Omega^* |\sin \lambda|}}, \quad (7)$$

and the velocity-scale,  $G$ , is used to construct our time-scale for non-dimensionalisation. With this choice, then

$$\text{Re} \equiv \frac{GD}{\nu} = \frac{1}{\Omega^* |\sin \lambda|}, \quad (8)$$

and

$$\text{Fr} \equiv \frac{G}{\sqrt{gD}}. \quad (9)$$

Finally, the non-dimensionalised potential temperature is defined as

$$\theta^* \equiv \frac{1}{\text{Fr}^2} \frac{\theta - \bar{\theta}}{\theta_0} \quad (10)$$

with thermal diffusion parameterised by  $\text{Pr} \equiv \nu/\kappa$ . For notational clarity, we will now drop all \*'s and from now on take each variable to be dimensionless.

## 2.2 Linearisation

We now linearise (5) about the laminar Ekman boundary layer basic state (Ekman, 1905), rotated through  $\varepsilon$ ,

$$U(z) = \cos \varepsilon - e^{-z} \cos(z + \varepsilon) \quad (11a)$$

$$V(z) = -\sin \varepsilon + e^{-z} \sin(z + \varepsilon) \quad (11b)$$

$$W(z) = 0 \quad (11c)$$

$$\bar{\theta}(z) = 0. \quad (11d)$$

Assuming Squire's theorem applies, we can now only consider two-dimensional perturbations in the rotated  $\hat{y} - \hat{z}$  plane  $\varepsilon + \pi/2$  north of the geostrophic wind. Then the normal modes can be written as

$$\psi = \phi(z)e^{ik(y-ct)} \quad (12a)$$

$$\tilde{u} = \chi(z)e^{ik(y-ct)} \quad (12b)$$

$$\Theta = \theta(z)e^{ik(y-ct)} \quad (12c)$$

where we have made a Helmholtz decomposition of the perturbation (tilde) variables with  $\tilde{w} \equiv \partial_y \psi = ik\phi$  and  $\tilde{v} \equiv -\partial_z \psi = -\mathcal{D}\phi$ . After eliminating pressure, the resulting eigenvalue problem may be concisely written as

$$\begin{aligned} & \begin{bmatrix} -\frac{(\mathcal{D}^2 - k^2)^2}{ik\text{Re}} + V(\mathcal{D}^2 - k^2) - V'' & -\frac{2(\mathcal{D} - ik\mu)}{ik\text{Re}} & -1 \\ U' + \frac{2(\mathcal{D} - ik\mu)}{ik\text{Re}} & -\frac{(\mathcal{D}^2 - k^2)}{ik\text{Re}} + V & 0 \\ \text{Ri}_l & 0 & V - \frac{(\mathcal{D}^2 - k^2)}{ik\text{RePr}} \end{bmatrix} \begin{bmatrix} \phi \\ \chi \\ \Theta \end{bmatrix} \\ & = c \begin{bmatrix} (\mathcal{D}^2 - k^2) & 0 & 0 \\ 0 & 1 & 0 \\ 0 & 0 & 1 \end{bmatrix} \begin{bmatrix} \phi \\ \chi \\ \Theta \end{bmatrix} \end{aligned} \quad (13)$$

where  $\mu \equiv -\cot \lambda \cos \beta$ .

We enforce rigid, no-slip, perfectly conducting boundaries at  $z = 0$ , and similarly with the geostrophic free-stream as  $z \rightarrow \infty$ . In the eigenvalue problem, this means that at  $z = 0$ , we require  $\phi = \mathcal{D}\phi = \chi = \Theta = 0$ . Similarly, as  $z \rightarrow \infty$ , we set  $\phi = \mathcal{D}^2\phi = \mathcal{D}\chi = \Theta = 0$ . For ease of validation comparing with Brown (1972), the following analysis will focus on the parameterisation with  $\text{Ri}_l$  constant in height, which then coincides with a bulk Richardson number. Although this thermal basic state is indeed artificial, to find a more realistic basic state requires considering the turbulent Ekman layer, and balancing radiative and turbulent thermal transport.

### 2.3 Continuous spectra

We now seek bounded solutions to the eigenvalue problem (13) which do *not* simply decay with increasing  $z$ , but rather take an oscillatory vertical profile (Grosch & Salwen, 1978). Although it is known that the discrete spectrum governs the time-asymptotic response of the perturbations introduced, we are interested in computing these continuous spectra analytically for validating the numerical implementation of the eigenvalue solver. These continuous spectra take on any vertical wavenumber,  $\lambda$ , which is the continuum parameter in this analysis. In the free-stream, the system of ODEs (13) takes on constant coefficients. Further, by assuming solution profiles like  $e^{i\lambda z}$  in the free-stream, then the linear algebraic system becomes

$$\begin{bmatrix} \frac{i(\lambda^2+k^2)^2}{k\text{Re}} - (V - \frac{\omega}{k})(\lambda^2 + k^2) & -\frac{2(\lambda-k\mu)}{k\text{Re}} & -1 \\ \frac{2(\lambda-k\mu)}{k\text{Re}} & V - \frac{i(\lambda^2+k^2)}{k\text{Re}} - \frac{\omega}{k} & 0 \\ \text{Ri}_l & 0 & V - \frac{i(\lambda^2+k^2)}{k\text{PrRe}} - \frac{\omega}{k} \end{bmatrix} = 0. \quad (14)$$

The determinant of this linear system gives the characteristic polynomial for  $k$  and  $\omega$ . The temporal continuous spectrum is solved by computing the 3 roots of the characteristic polynomial in terms of  $\omega$ , thus giving the three branches of the continuous spectrum for  $\omega(\lambda; k) \in \mathbb{C}$ . Assuming for now that  $\text{Pr} = 1$  at latitude  $90^\circ$  such that  $\mu = 0$ , then the temporal spectra can be written explicitly as

$$\omega_0 = kV_\infty - i\frac{k^2 - \lambda^2}{\text{Re}} \quad (15)$$

$$\omega_\pm = kV_\infty \pm \frac{1}{\text{Re}} \sqrt{\frac{k^2\text{Re}^2\text{Ri} - 4\lambda^2}{k^2 - \lambda^2}} - i\frac{k^2 - \lambda^2}{\text{Re}} \quad (16)$$

where  $V_\infty = -\sin \varepsilon$ . For the more general case without a restricted  $\text{Pr}$  and latitude,  $\text{Det}[(14)] = 0$  may be solved numerically with a fast polynomial root-finding algorithm.

Alternatively, solving the characteristic equation rather for the 8<sup>th</sup> order polynomial in  $k$ , gives 8 roots for  $k(\lambda; \omega) \in \mathbb{C}$ . Each of these roots may be similarly computed numerically with a polynomial root finding algorithm; however, only 4 of the roots correspond to modes propagating in  $x > 0$  and are relevant to our following spatial stability analysis. It should be noted that in this continuous spatial analysis, and the following discrete spatial spectrum, the direction of spatial growth has been implicitly assumed to be aligned with the propagation direction (i.e.  $\hat{y}$ ) by our change of coordinates.

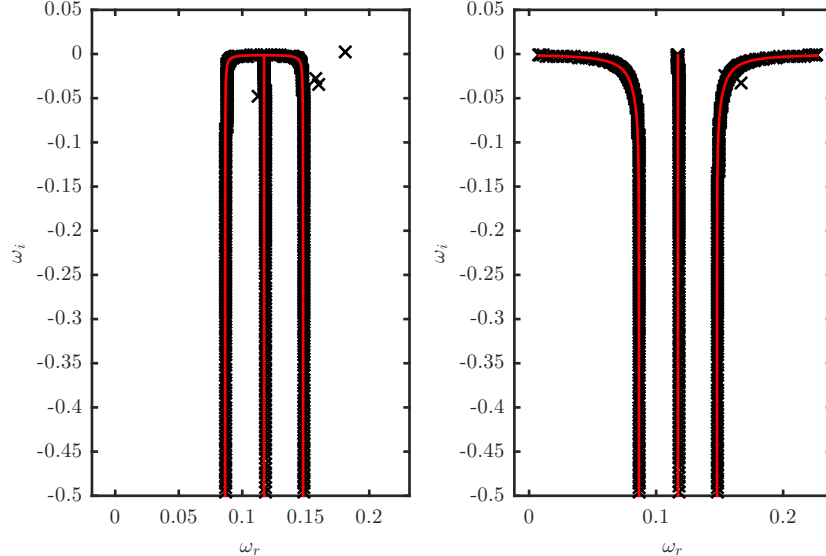


Figure 1: Comparison of the temporal discrete spectrum with the continuous spectrum for marginal stability at  $\text{Re} = 65$ ,  $\text{Pr} = 0.7$ , and  $\varepsilon = -23$ , with perturbations  $k = 0.3$ . On the right, shown without stratification, and at left with  $\text{Ri}_l = 0.012$ .

### 3 Numerical model

#### 3.1 Discrete temporal spectrum

The discrete temporal spectrum to the linear eigenvalue problem (13) is solved numerically using a mapped Chebyshev pseudo-spectral collocation method. The physical problem domain is semi-infinite, however, in this implementation, we use a vertical domain size of 30 times the Ekman layer depth. The resulting matrix system to be solved is of size  $3N$ , and good convergence has been shown on the finite interval,  $[0, z_{\text{top}}]$ , for both  $N = 256$  and  $z_{\text{top}} = 30$  with typical parameter values.

We have validated the temporal growth rates over the  $k$ - $\varepsilon$  parameter space, against the linearly stratified Ekman stability analysis of Brown (1972) at  $\text{Ri}_l = 0.012$  and  $\text{Re} = 900$ . We find good agreement with the Type I mode of instability, however their limited search employing the shooting method meant that they did not find the stationary (Type II) mode active in particular  $\varepsilon < 0$ .

We further verify that the vertically bounded eigenvectors correspond with eigenvalues falling on the continuous spectrum found in §2.3. However, to find good convergence onto the continuous spectrum, a much larger vertical domain height of  $z_{\text{top}} = 120$  is required. The marginally unstable Type II mode for  $\text{Pr} = 0.7$  at  $\text{Re} = 65$ , located at  $k = 0.3$  and  $\varepsilon = -23$ , is shown in Fig. 1.

### 3.2 Discrete spatial spectrum

The discrete spatial eigenvalue problem can be formulated by rearranging (13) with  $k$  as the eigenvalue, thus resulting in a 4<sup>th</sup> order polynomial eigenvalue problem. Using a method similar to Bridges & Morris (1984), we decompose the 4<sup>th</sup> order  $3N \times 3N$  system into a linear  $12N \times 12N$  system, which may be solved in much the same way as §3.1. However, Landau & Lifshitz (1959) were the first to recognise that discerning spatial instability is not as trivial as finding any  $k_i < 0$  as in the temporal case for  $\omega_i$ . In addition to a positive imaginary component of the eigenvalue, the causality condition must also be satisfied, forming the basis of the criterion by Briggs (1964). The Briggs test is thus able to discern between spatially growing modes for  $x > 0$  and spatially decaying modes for  $x < 0$ , both of which have negative imaginary eigenvalues. This reality check for causality effectively introduces a damping term (by a negative imaginary contribution to the parameter  $\omega$ ) and ensures that the roots corresponding to  $x > 0$  indeed move to the upper-half plane of  $k$ , since they should also be spatially damped!

A numerical implementation of the Briggs causality test requires correlating successive solutions of the polynomial eigenvalue problem with the slight change in  $\omega_i$ . This is because algorithms used to compute eigenvalues generally have no guarantee of keeping the ordering consistent even with this small parameter change. Thus to follow the evolution of the eigenvalue spectrum, we have modified the Kuhn–Munkres assignment algorithm (Kuhn, 1955) for rectangular matrices, which generates a correlation matrix based on defined cost functions of the eigenvectors and eigenvalues. After correlating the successive solves of the spatial eigenspectrum, we then search for any  $k_i < 0$  *conditional on* satisfying temporal causation — i.e. migrating eigenvalues from  $k_i < 0$  to  $k_i > 0$  as the imaginary component of  $\omega$  increases.

It should be noted that with the addition of some imaginary term  $i\sigma$  to  $\omega$ , this value of  $\sigma$  which gives a root at the real  $k$ -axis crossing is indeed the temporal growth rate from §3.1! This implies that in order to have the possibility of spatial instability, the flow must first be unstable in a temporal sense for real  $k$ .

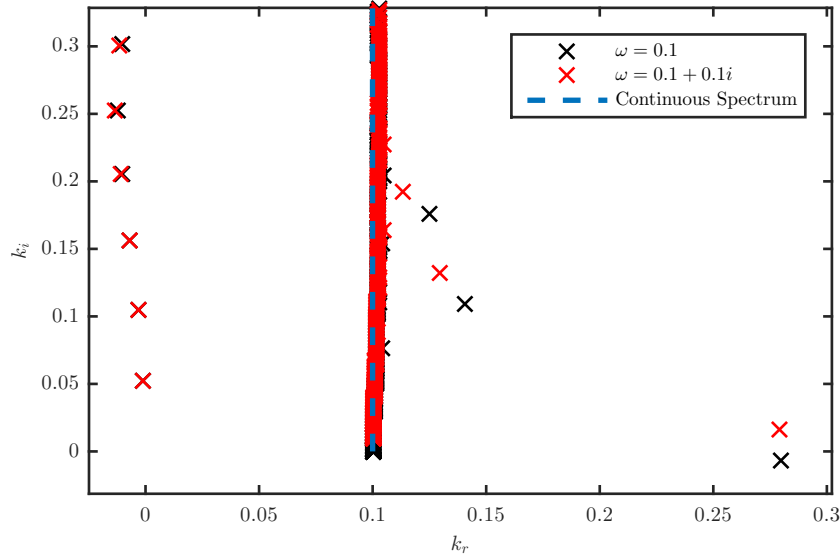


Figure 2: Spatio-temporal stability validation for the simple case of a Blasius boundary layer.

### 3.2.1 Reduction to Blasius

We first validate the full stratified spatial stability solver implemented by reduction to the Blasius boundary layer which has a known solution. This simplification does not, however, reduce the 4<sup>th</sup> order eigenvalue problem, and so is a good initial test. By setting  $\Omega = 0$ , and further using the Blasius profile for  $V$ , we ensure agreement with the continuous spectrum analytically found by Grosch & Salwen (1978), and presented for  $\text{Re} = 1000$  and  $\omega = 0.1$  in Fig. 2. We further compare the corresponding eigenvalues with those found using a modified shooting method by Jacobs & Durbin (1998). We also validate against the resulting discrete spectrum computed by Sengupta et al. (2011) for this marginally stable case, and find agreement to within 0.1% error.

### 3.2.2 Unstratified Ekman layer

We continue the validation of our numerical spatial stability solver by comparing against known marginally spatially unstable unstratified Ekman layer results (Marlatt & Biringen, 1994). They apply the Gaster transformation after solving the temporal problem to compute a neutral stability curve.

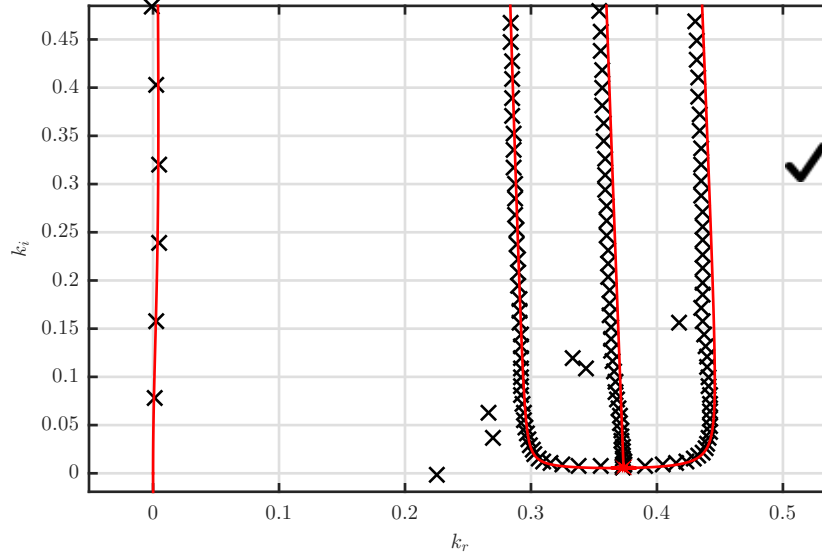


Figure 3: Validation of the spatial spectrum for an unstratified marginally stable Ekman layer ( $\text{Re} = 65$ ,  $\varepsilon = -23$ , and  $\omega = 0.146$ ). Shown along with the analytically computed continuous spectrum.

Taking parameters  $\text{Re} = 65$ ,  $\varepsilon = -23$ , and  $\omega = 0.146$ , we indeed capture neutral spatial stability as shown by the eigenvalue on the  $k_r$  axis in Fig. 3. It is also apparent from this figure that even with  $N = 128$  and  $z_{\text{top}} = 30$ , that all four positive branches of the spatial continuous spectrum are well-captured. It should be noted that the discrete eigenvalues converge much more quickly as the corresponding eigenvectors decay far away from the artificially-constrained domain.

### 3.2.3 Stratified continuous spectrum

We finish validating this implementation by comparing the numerically computed spatial continuous spectrum for the stratified Ekman layer to that found analytically in §2.3. To help ensure the full generality of this code is correct, we conduct this comparison additionally for various combinations of  $\mu$  and  $\text{Pr}$ . With these additional degrees of freedom, and far from marginal stability, quite elaborate behaviour is observed in the continuous spectra as apparent in Fig. 3. The Briggs test applied to the case shown in this figure nonetheless still captures the single temporally unstable  $k = 0.3$  mode!

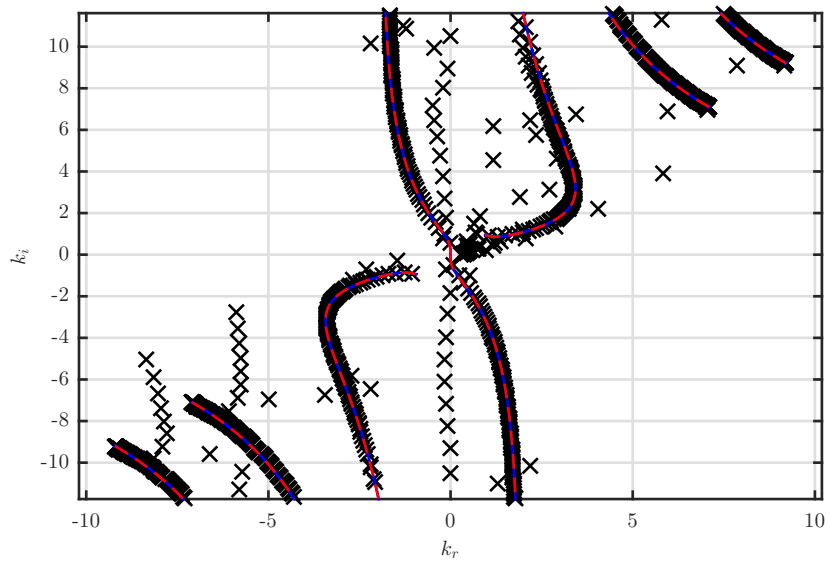


Figure 4: Validation of the stratified spatial continuous spectrum, shown here for the particular case of  $Re = 900$ ,  $Pr = 0.7$ ,  $Ri_l = 0.012$ ,  $\varepsilon = 0$ ,  $\omega = 0.112$ , and  $\mu = -0.5$  corresponding to a thoroughly unstable Type II instability.

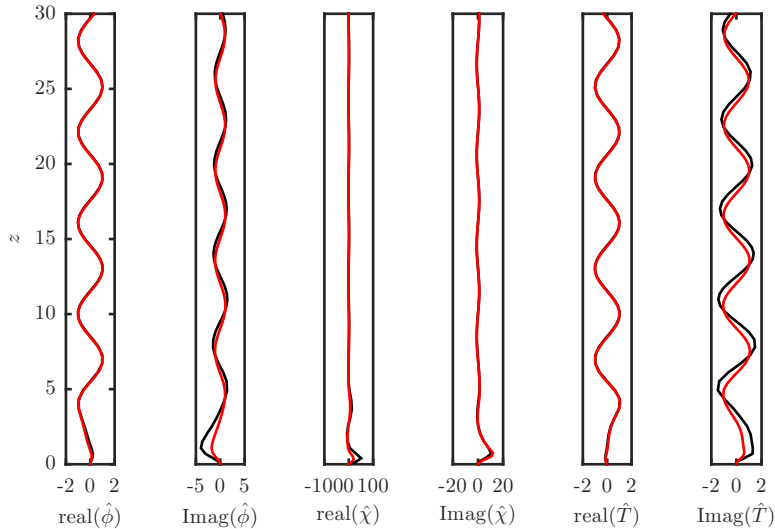


Figure 5: Comparison of a particular eigenvector on the continuous spatial spectrum for  $z_{\text{top}} = 60$  (black), and  $z_{\text{top}} = 60 + 8\pi\lambda$  (red).

With assurance that the continuous spectrum is consistent, we also must ensure that the corresponding eigenfunctions are correct. Any free-stream perturbation projects entirely onto these continuous modes, and so for considerations of bypass transition via mode-coupling with the discrete spectrum, these continuous eigenfunctions are required to be accurate. To this end, we compare corresponding eigenfunctions with increasing height to gauge any effects of the finite boundary height. We increase the domain size by  $8\pi\lambda$ , such that in the limit as  $z_{\text{top}} \rightarrow \infty$  the additional domain height remains exactly commensurate as the previous domain for the particular free-stream vertical wavenumber,  $\lambda$ . These eigenfunctions are shown in Fig. 5, where it is apparent that the slight mismatch in the free-stream wavenumber not yet being exactly commensurate with  $\lambda$  causes small deviations in the near-wall region.

## 4 Results

Although stratification contributes an additional degree of freedom, and thus another dynamical mode for instability, stable stratification still has an overall damping effect on the susceptibility of laminar Ekman layers to both global perturbations and localised impulses. As an example, we fol-

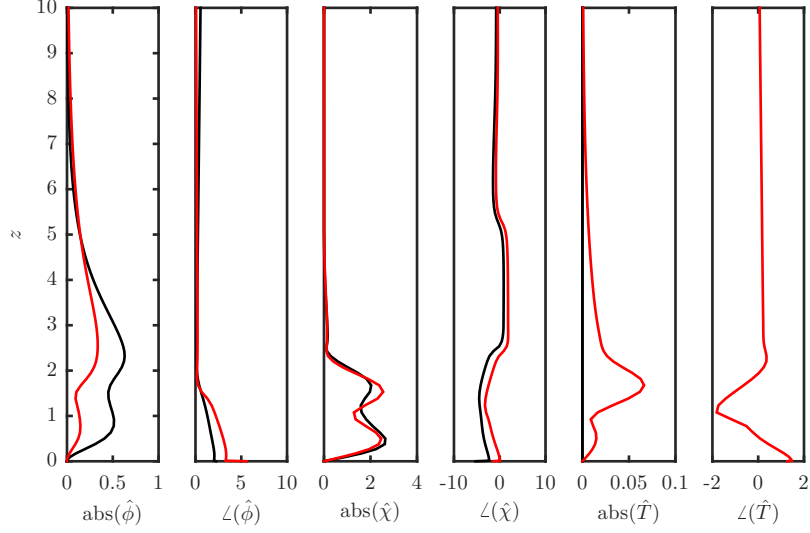


Figure 6: Comparison of the eigenfunctions for the unstratified (black) and stratified (red) Ekman layers. The additional thermal perturbation reduces the necessary velocity perturbations near the ground.

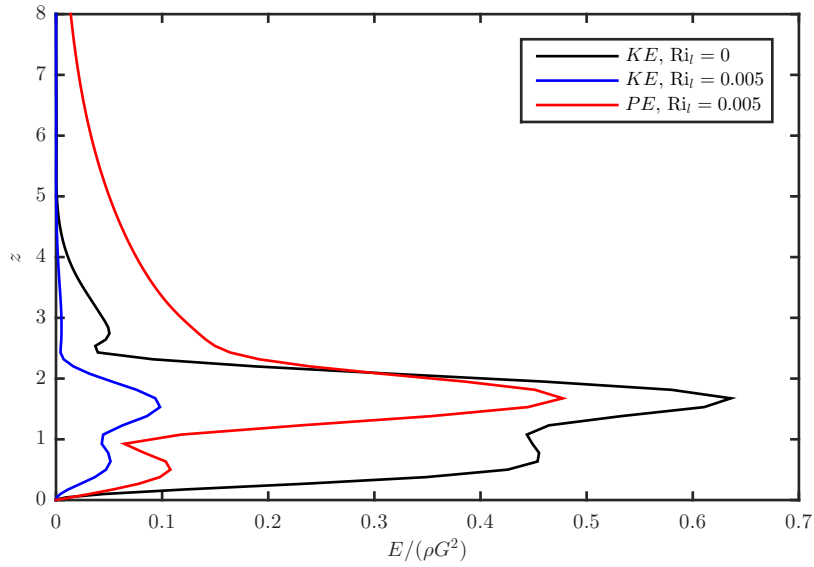


Figure 7: Kinetic energy in the spatially unstable unstratified mode, compared against the partitioned potential and kinetic energy in the same mode damped by stratification.

low the most spatio-temporally unstable mode in the problem from Fig. 4, while continuously increasing the linear stratification. The Ekman layer regains marginal spatial stability once  $\text{Ri}_l = 0.005$ , which produces a spatial structure with  $k = 0.6$ . Nonetheless, the boundary layer remains temporally unstable at this stratification. The influence stratification has on the eigenfunction profiles is shown in Fig. 6. With the introduction of stratification, the additional degree of freedom in the thermal equation partitions the perturbation energy, resulting in reduced relative eigenfunction contributions within the first few Ekman depths. From the linearised system, we can write the specific perturbation kinetic energy to be

$$\frac{KE}{\rho} = U|\chi| + V|\mathcal{D}\phi| \quad (17)$$

and in the stratified case, the gravitational potential energy arising from adiabatic thermal perturbations is

$$\frac{PE}{\rho} = \frac{|\theta|}{\text{Ri}_l}. \quad (18)$$

Thus for a budget of input energy, the stratified Ekman layer must partition this energy between an additional degree of freedom, thus reducing the dynamic terms in the instability. This is apparent in Fig. 7, which shows the relative contributions of potential and kinetic perturbation energy normalised by the total energy.

#### 4.1 Temporal growth

We first lay the landscape for the linear temporal growth at the North Pole as a function of the perturbation wavenumber ( $k$ ) and  $\varepsilon$ , which is displayed in Fig. 8. In the absence of stratification, it is apparent that the inflectional (and stationary) Type I mode is dominant, even though the Type II mode has a lower threshold  $\text{Re}$ . As pointed out by Allen & Bridges (2003), this is indeed an inviscid crossflow-type instability arising due to an inflection point in the velocity profile. We verify this observation by ensuring that the group velocity is very small,  $v_g \sim 0.01$  for typical parameters. With increasing stratification, each of these modes of instability are damped; however, it should be noted that although the Type I mode achieves faster growth in the case shown in Fig. 9, the Type II mode remains more resilient with further increasing stratification. This Type II (“parallel”) travelling wave mode was first found by Lilly (1966), and has since been determined to be a viscous-type instability similar to that of Tollmien–Schlichting waves.

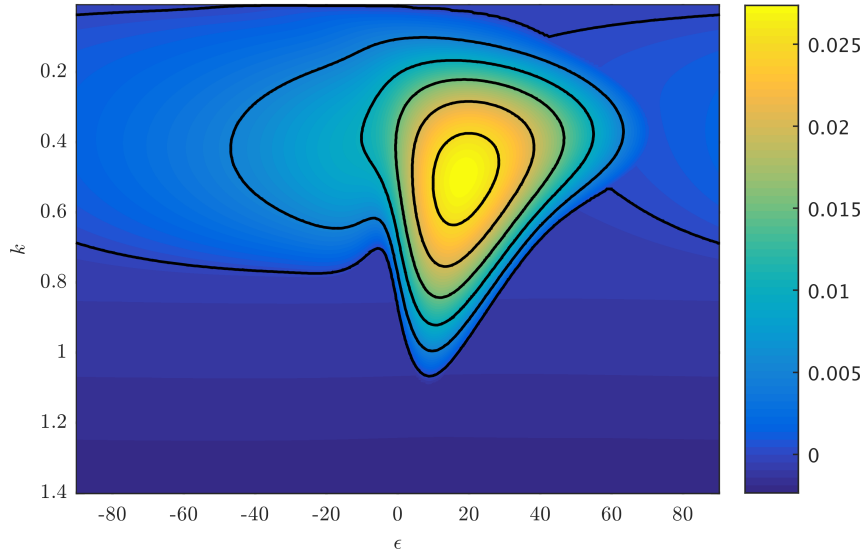


Figure 8: Temporal stability diagram for the unstratified Ekman layer with  $Re = 900$  and  $Pr = 1$ . The outer contour indicates the neutral stability curve.

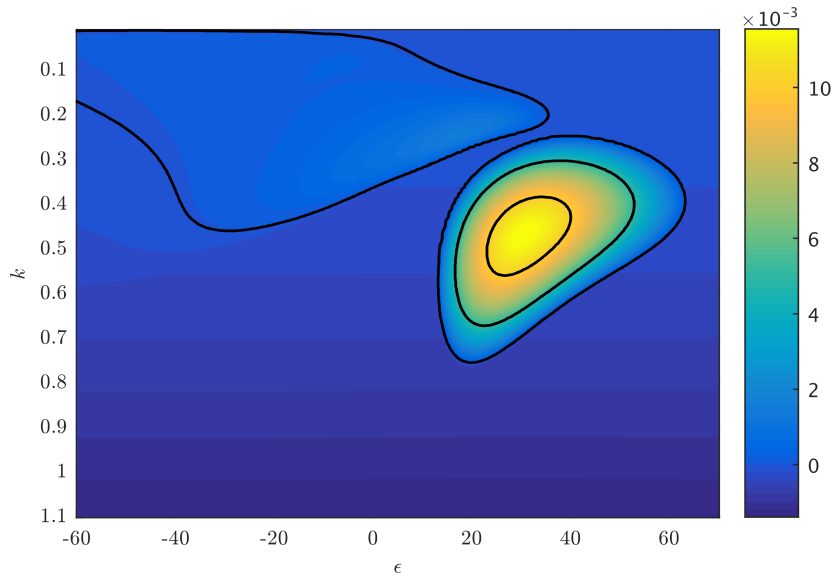


Figure 9: Temporal stability diagram for the stratified Ekman layer with  $Ri_l = 0.012$ , for  $Re = 900$  and  $Pr = 1$ .

Furthermore, similar to the semi-infinite Blasius boundary layer discrete spectrum, we find that the stratified Ekman layer has only a finite and small (yet increasing with  $\text{Re}$ ) number of discrete eigenvalues. This was shown numerically for the Blasius boundary layer (Mack, 1976), but contrasts with the infinite discrete spectrum in channel flow. In a similar fashion to Mack, we numerically show a finite discrete spectrum for a sufficient number of parameter pairs to build confidence in this conclusion.

## 4.2 Spatial growth

We now extend the temporal stability to explore the neutral stability of spatial perturbations specifically growing in the direction  $\epsilon$ . Fig. 10 shows this unstratified spatial stability diagram over a range of localised perturbation frequencies,  $\omega$ . One might expect mirror symmetry in this diagram at the North Pole (as in the temporal case); however, this only holds when maximising the growth over all directions, rather than restricting to the  $\tilde{y}$  direction. The geostrophic flow thus breaks the isotropy in this case because for  $\epsilon > 0$ , the rotated  $\tilde{y}$  coordinate has a component into the geostrophic wind. Thus, because it was implicitly assumed that the growth and phase propagation direction coincide, then we could expect the spatial growth to be damped for most  $\epsilon > 0$  as shown. This observation further motivates the necessity for allowing the additional degree of freedom to prescribe the growth direction of interest, as was done by Lu & Lele (1993) for the stability of a skewed mixing layer. Nonetheless, as in the temporal case, with stratification (amounting to  $\text{Ri}_l$ ) each unstable mode is damped by at least a factor of 100. We have also found no clear distinction between different characters of the modes of instability as in the temporal case.

## 5 Conclusion & Future Work

We have analytically found the temporal and spatial continuous spectra for a generalised laminar stratified Ekman layer. We further computed the discrete spatial spectrum and conclude that, similar to the Blasius boundary layer, only a finite set of eigenvalues belong to the discrete spectrum of the stratified Ekman layer. We extend the current literature by designing a numerical algorithm to quickly correlate and track the evolution of all eigenvalues, and thus determine spatial stability. The inclusion of linear stratification indeed stabilises the Ekman layer both to temporal instability and also spatial instability with localised perturbations.

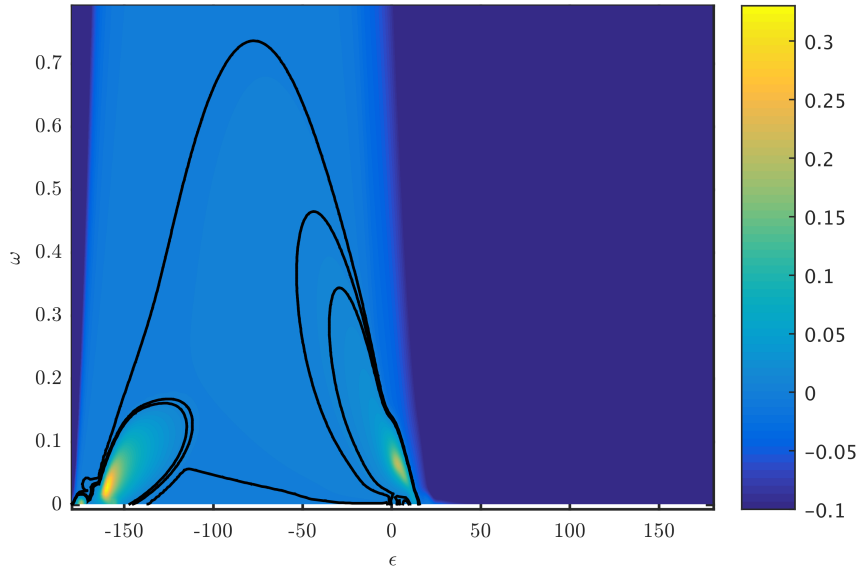


Figure 10: Spatial stability diagram for the unstratified Ekman layer with  $Re = 900$  and  $Pr = 1$ .  $\varepsilon > 0$  corresponds to propagation in the up-stream direction and thus stability is expected.

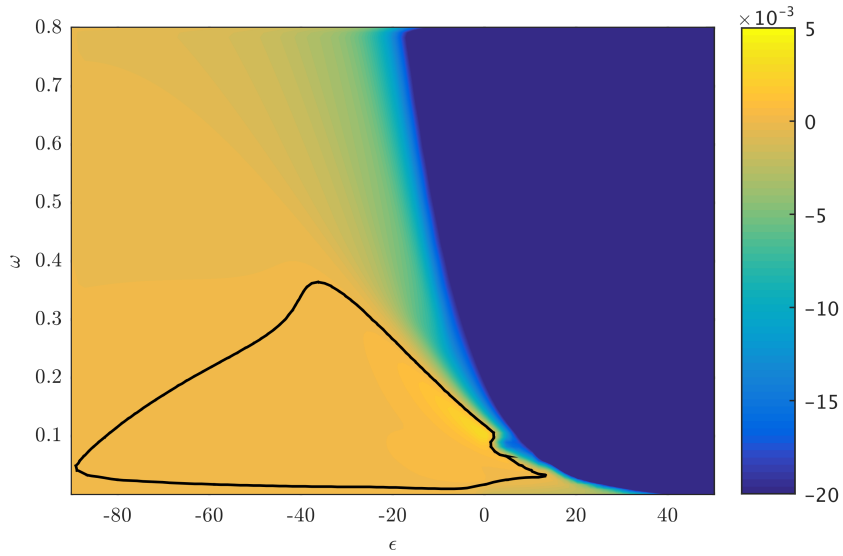


Figure 11: Spatial stability diagram for the stratified Ekman layer with  $Ri_l = 0.012$ , for  $Re = 900$  and  $Pr = 1$ .

Future work will further generalise this developed linear theory to open another degree of freedom allowing the amplification direction and phase propagation direction to differ. While irrelevant to the temporal stability analysis, this work has made it apparent that the restriction of  $k_x = 0$  does not allow the maximum spatial growth to be captured. We will additionally evolve local spatial perturbations using large-eddy simulation to help motivate this endeavour as well as validate the spatial growth results in the stratified Ekman layer in the  $\tilde{y}$  direction. Onto the signalling problem, these simulations will also guide further study into how these wave forms may travel separately from the group velocities.

The effects of realistic temperature inversion profiles will also be explored in future work, as this is expected to have a strong effect on the character of the propagating waves. Below the inversion in the unstratified region, internal gravity waves are not supported, yet above the inversion jump after regaining a typical thermal lapse rate then this additional mode becomes available. We will also seek optimal perturbations and explore non-modal spatial growth, as each could eventually be exploited in the wind farm configuration engineering community to improve mixing or mitigate wake effects in arrays of wind turbines. Finally, an extension of this analysis in an turbulence-averaged formalism will help to generalise our results to realistic turbulent Ekman layers.

## References

- Allen L., Bridges T. J., 2003, European Journal of Mechanics - B/Fluids, 22, 239
- Ashpis D. E., Reshotko E., 1990, Journal of Fluid Mechanics
- Bridges T. J., Morris P. J., 1984, Journal of Computational Physics, 55, 437
- Briggs R. J., 1964, Electron-Stream Interaction with Plasmas. MIT Press
- Brown R. A., 1972, Journal of the Atmospheric Sciences
- Ekman V. W., 1905, Arkiv för matematik, astronomi och fysik, 2, 1
- Gaster M., 1962, Journal of Fluid Mechanics, 14, 222
- Gaster M., 1965, Progress in Aerospace Sciences, 6, 251
- Grosch C. E., Salwen H., 1978, Journal of Fluid Mechanics, 87, 33

- Jacobs R. G., Durbin P. A., 1998, *Physics of Fluids*, 10, 2006
- Kuhn H. W., 1955, *Naval Research Logistics Quarterly*, 2, 83
- Landau L. D., Lifshitz E. M., 1959, *Fluid Dynamics (Course of Theoretical Physics vol VI)*
- Lilly D. K., 1966, *Journal of the Atmospheric Sciences*, 23, 481
- Lu G., Lele S. K., 1993, *Journal of Fluid Mechanics*, 249, 441
- Mack L. M., 1976, *Journal of Fluid Mechanics*
- Marlatt S. W., Biringen S., 1994, *Journal of the Atmospheric Sciences*
- Sengupta T. K., Unnikrishnan S., Bhaumik S., Singh P., Usman S., 2011, *Progress in Applied Mathematics*, 1, 71